

The Composite Spectrum of QSO Absorption Line Systems in DESI DR2

LUCAS NAPOLITANO,¹ ADAM D. MYERS,¹ ADAM TEDESCHI,¹ ABHIJEET ANAND,² HIRAM K. HERRERA-ALCANTAR,^{3,4}
JESSICA AGUILAR,² STEVEN AHLEN,⁵ STEPHEN BAILEY,² SEGEV BENZVI,⁶ DAVIDE BIANCHI,^{7,8} DAVID BROOKS,⁹
TODD CLAYBAUGH,² ANDREI CUCEU,² AXEL DE LA MACORRA,¹⁰ ARJUN DEY,¹¹ BIPRATEEP DEY,^{12,13} PETER DOEL,⁹
ANDREU FONT-RIBERA,¹⁴ JAIME E. FORERO-ROMERO,^{15,16} ENRIQUE GAZTAÑAGA,^{17,18,19} SATYA GONTCHO A GONTCHO,^{2,20}
GASTON GUTIERREZ,²¹ JULIEN GUY,² DICK JOYCE,¹¹ ANTHONY KREMIN,² MARTIN LANDRIAU,² LAURENT LE GUILLOU,²²
MARC MANERA,²³ AARON MEISNER,¹¹ RAMON MIQUEL,^{24,14} JOHN MOUSTAKAS,²⁵ SESHADRI NADATHUR,¹⁸
NATHALIE PALANQUE-DELABROUILLE,^{4,2} WILL PERCIVAL,^{26,27,28} FRANCISCO PRADA,²⁹ IGNASI PÉREZ-RÀFOLS,³⁰
GRAZIANO ROSSI,³¹ EUSEBIO SANCHEZ,³² DAVID SCHLEGEL,² MICHAEL SCHUBNEL,^{33,34} JOESPH HARRY SILBER,²
DAVID SPRAYBERRY,¹¹ GREGORY TARLÉ,³⁴ BENJAMIN ALAN WEAVER,¹¹ RONGPU ZHOU,² AND HU ZOU³⁵

¹Department of Physics & Astronomy, University of Wyoming, 1000 E. University, Dept. 3905, Laramie, WY 82071, USA

²Lawrence Berkeley National Laboratory, 1 Cyclotron Road, Berkeley, CA 94720, USA

³Institut d'Astrophysique de Paris. 98 bis boulevard Arago. 75014 Paris, France

⁴IRFU, CEA, Université Paris-Saclay, F-91191 Gif-sur-Yvette, France

⁵Physics Dept., Boston University, 590 Commonwealth Avenue, Boston, MA 02215, USA

⁶Department of Physics & Astronomy, University of Rochester, 206 Bausch and Lomb Hall, P.O. Box 270171, Rochester, NY 14627-0171, USA

⁷Dipartimento di Fisica “Aldo Pontremoli”, Università degli Studi di Milano, Via Celoria 16, I-20133 Milano, Italy

⁸INAF-Osservatorio Astronomico di Brera, Via Brera 28, 20122 Milano, Italy

⁹Department of Physics & Astronomy, University College London, Gower Street, London, WC1E 6BT, UK

¹⁰Instituto de Física, Universidad Nacional Autónoma de México, Cd. de México C.P. 04510, México

¹¹NSF NOIRLab, 950 N. Cherry Ave., Tucson, AZ 85719, USA

¹²Department of Astronomy & Astrophysics, University of Toronto, Toronto, ON M5S 3H4, Canada

¹³Department of Physics & Astronomy and Pittsburgh Particle Physics, Astrophysics, and Cosmology Center (PITT PACC), University of Pittsburgh, 3941 O'Hara Street, Pittsburgh, PA 15260, USA

¹⁴Institut de Física d'Altes Energies (IFAE), The Barcelona Institute of Science and Technology, Campus UAB, 08193 Bellaterra Barcelona, Spain

¹⁵Departamento de Física, Universidad de los Andes, Cra. 1 No. 18A-10, Edificio Ip, CP 111711, Bogotá, Colombia

¹⁶Observatorio Astronómico, Universidad de los Andes, Cra. 1 No. 18A-10, Edificio H, CP 111711 Bogotá, Colombia

¹⁷Institut d'Estudis Espacials de Catalunya (IEEC), 08034 Barcelona, Spain

¹⁸Institute of Cosmology and Gravitation, University of Portsmouth, Dennis Sciama Building, Portsmouth, PO1 3FX, UK

¹⁹Institute of Space Sciences, ICE-CSIC, Campus UAB, Carrer de Can Magrans s/n, 08913 Bellaterra, Barcelona, Spain

²⁰University of Virginia, Department of Astronomy, Charlottesville, VA 22904, USA

²¹Fermi National Accelerator Laboratory, PO Box 500, Batavia, IL 60510, USA

²²Sorbonne Université, CNRS/IN2P3, Laboratoire de Physique Nucléaire et de Hautes Energies (LPNHE), FR-75005 Paris, France

²³Departament de Física, Serra Hünter, Universitat Autònoma de Barcelona, 08193 Bellaterra (Barcelona), Spain

²⁴Institució Catalana de Recerca i Estudis Avançats, Passeig de Lluís Companys, 23, 08010 Barcelona, Spain

²⁵Department of Physics and Astronomy, Siena College, 515 Loudon Road, Loudonville, NY 12211, USA

²⁶Department of Physics and Astronomy, University of Waterloo, 200 University Ave W, Waterloo, ON N2L 3G1, Canada

²⁷Perimeter Institute for Theoretical Physics, 31 Caroline St. North, Waterloo, ON N2L 2Y5, Canada

²⁸Waterloo Centre for Astrophysics, University of Waterloo, 200 University Ave W, Waterloo, ON N2L 3G1, Canada

²⁹Instituto de Astrofísica de Andalucía (CSIC), Glorieta de la Astronomía, s/n, E-18008 Granada, Spain

³⁰Departament de Física, EEBE, Universitat Politècnica de Catalunya, c/Eduard Maristany 10, 08930 Barcelona, Spain

³¹Department of Physics and Astronomy, Sejong University, Seoul, 143-747, Korea

³²CIEMAT, Avenida Complutense 40, E-28040 Madrid, Spain

³³Department of Physics, University of Michigan, Ann Arbor, MI 48109, USA

³⁴University of Michigan, Ann Arbor, MI 48109, USA

³⁵National Astronomical Observatories, Chinese Academy of Sciences, A20 Datun Rd., Chaoyang District, Beijing, 100012, P.R. China

ABSTRACT

We present details regarding the construction of a composite spectrum of quasar (QSO) absorption line systems. In this composite spectrum we identify more than 70 absorption lines, and observe oxygen and hydrogen emission features at a higher signal-to-noise ratio than in any previous study. As the light from a distant quasar travels towards an observer, it may interact with the circumgalactic medium environment of an intervening galaxy, forming absorption lines. In order to maximize the signal of these absorption lines, we have selected a sample of 238,838 quasar spectra from the second data release of the Dark Energy Spectroscopic Instrument (DESI), each identified to have absorption lines resulting from such an interaction. By stacking these spectra in the restframe of the absorption, and calculating a median composite spectrum, we are able to isolate and enhance these absorption lines. We provide a full atlas of all detected absorption and emission lines as well as their fit centroids and equivalent width values. This atlas should aid in future studies investigating the compositions and physical conditions of these absorbers.

1. INTRODUCTION

Shortly following the discovery of quasars (or “QSOs”) in the early 1960s (e.g. [Matthews & Sandage 1963](#); [Schmidt 1963](#)), absorption lines were identified in their spectra at redshifts distinct from that of their emission. [Wagoner et al. \(1967\)](#) and [Bahcall & Spitzer \(1969\)](#) were among the first to propose that these lines were caused by interactions with gas in the extended halos, i.e. the circumgalactic environments (CGM), of intervening galaxies that were within the line of sight to the more distant quasar. Studies of the CGM are summarized in [Tumlinson et al. \(2017\)](#).

Absorption lines in QSO spectra are commonly divided into two groups, parameterized by the velocity offset between the background QSO and foreground absorption environment, as determined using their respective redshifts:

$$v_{\text{off}} = c \frac{z_{\text{QSO}} - z_{\text{ABS}}}{1 + z_{\text{QSO}}} \quad (1)$$

Although the exact transition in velocity space between different types of absorbers is a complex matter, absorbers at $v_{\text{off}} > 3,500 \text{ km s}^{-1}$ are generally considered to be intervening absorbers, whereas those systems at velocity offsets less than 3500 km s^{-1} are considered to be “associated” with the QSO host galaxy (e.g. [York et al. 2006](#); [Zhu & Ménard 2013](#); [Khare et al. 2014](#); [Chen et al. 2020](#); [Lan 2020](#); [Anand et al. 2021](#); [Wu et al. 2025](#)).

The host galaxies of the circumgalactic environments that result in intervening absorption line systems are commonly too dim to be observed, particularly those at redshifts beyond $z = 1$ (e.g. [Frank et al. 2012](#); [Corlies & Schiminovich 2016](#); [Corlies et al. 2020](#); [Wijers & Schaye 2022](#)). As such, the produced absorption lines are one of very few methods by which we can gain insight into the gas content and other physical characteristics of these galactic environments.

The construction of median composite spectra is a technique frequently used in astronomy. By combining

a large sample of similar objects and determining the median value at each wavelength value, one can reveal common features, and significantly increase signal-to-noise (e.g. [Francis et al. 1991](#); [Zheng et al. 1997](#)). In the world of large sky surveys, composite quasar spectra are frequently calculated in order to study emission or absorption line characteristics (e.g. [Brotherton et al. 2001](#); [Vanden Berk et al. 2001, 2008](#); [Alam et al. 2021](#)), to characterize spectral energy distributions (e.g. [Sambruna et al. 1996](#); [Richards et al. 2006](#); [Mullaney et al. 2011](#)), and to determine the nature of different classes of quasars such as red quasars (e.g. [Selsing et al. 2016](#); [Fawcett et al. 2023](#)) or BAL quasars (e.g. [Sprayberry & Foltz 1992](#); [Gallagher et al. 2007](#)).

In this paper we calculate the composite spectrum of a large set of intervening absorption line systems. By shifting the QSO spectra that host these intervening absorbers into the restframe of their absorption, we are able to remove both the obscuring effect of the broad emission lines of the QSO, as well as reduce the innate noise in the individual data. Similar studies have been performed in order to search for high ionization state absorption lines ([Lu & Savage 1993](#)), or to characterize the physical conditions and metal enrichment of the intergalactic medium ([York et al. 2006](#); [Pieri et al. 2010](#)), or to explore the physical properties of intervening Mg II gas clouds (e.g. [Zhu & Ménard 2013](#); [Khare et al. 2014](#); [Lan & Fukugita 2017](#); [Chen et al. 2020](#); [Anand et al. 2021](#)).

A number of studies that utilize absorber composite spectra further investigate the relationship between Mg II absorbers, and star formation, in both the case of associated, and intervening absorption systems. [Wild et al. \(2007\)](#) utilized composites constructed with both Ca II and Mg II absorbers to detect the [O II] 3727, 3730Å emission lines. This result was expanded upon in [Ménard et al. \(2011\)](#) which demonstrated a relationship between the rest-frame equivalent width of Mg II absorbers and the star formation rate, as measured us-

ing the [O II] lines (see also López & Chen (2012)). This relationship is further investigated in the papers Shen & Ménard (2012); Khare et al. (2014); Joshi et al. (2018) generally using samples of associated absorption systems.

A similar analysis of galaxies in the foreground of QSO spectra was carried out in the Sloan Digital Sky Survey (e.g. York et al. 2012; Straka et al. 2013, 2015). By detecting sets of QSO-galaxy pairs observed in the same fiber these studies were able to measure the emission features directly in individual spectra without the need for composite spectra.

Absorber composite studies commonly utilize a catalog of absorbers formed based on the detection of a single high-signal absorption species. The choice of this high-signal species is significant as it, along with the wavelength coverage of the spectra utilized, determine the wavelength coverage of the computed composite spectra. In this study we choose to utilize an input catalog of Mg II absorbers (Napolitano et al. 2023) detected in spectra collected by the Dark Energy Spectroscopic Instrument (DESI) (DESI Collaboration et al. 2016, 2022; Guy et al. 2023a; Miller et al. 2024; Poppett et al. 2024). Details regarding the daily operations of the DESI survey are presented in Schlafly et al. (2023).

DESI has recently completed the processing of its second data release, containing spectra from the first three years of the survey (DESI Collaboration et al. 2025a,b). The QSO catalog produced using this data release has a total of 2,456,178 entries, and the details of their selection and cataloging are given in Chaussidon et al. (2023) and Alexander et al. (2023). Note that we restrict our parent QSO sample to only those spectra that were originally targeted as QSOs in the interest of sample purity. The Mg II absorption system catalog constructed from this parent QSO sample has a total of 545,905 entries, detected in 394,561 total spectra, and its construction is detailed in Napolitano et al. (2023) and Napolitano et al. (2025).

In this paper we will utilize this sample in order to construct an extremely high signal-to-noise QSO absorption line system composite. From this composite, we will create an atlas of detected emission and absorption species and measure their centroids relative to catalog values, as well as their equivalent width values. In doing so, we will provide a more complete understanding of these systems than has previously been possible.

This paper will be organized in the following fashion: In §2 we will detail the construction of the absorber composite including our sample selection and the composite construction methodology. In §3 we will consider the composite, measuring all detected lines with a particu-

lar focus on the emission features we find. In §4 we will discuss applications of this composite, as well as verifying the nature of the emission features and considering their significance. In §5 we present our conclusions.

2. DATA METHODS

In this section we will outline the selection of our sample of intervening absorption systems, as well as that of our control sample of QSOs with no absorption systems. We will then detail the methods by which we construct our median composite spectrum, and the methods by which we identify and fit the absorption lines present in the composite spectrum.

2.1. Sample Selection

First we must note that late in the preparation of this manuscript a bug was discovered in the Mg II detection pipeline that produced the catalog used in this analysis. This bug resulted in a number of possible doublet candidates, with line separations too narrow to be Mg II, being incorrectly passed to the MCMC fitting stage of our detection procedure. The majority of these erroneously considered absorber candidates were later rejected on the basis of the quality cuts described in Napolitano et al. (2023), however a small number can still be found in the currently existing catalogs.

When reconstructing the DESI DR2 catalog following the resolution of this bug, the total sample size decreases from 545,905 entries to 539,151, a percentage decrease slightly greater than 1%. As the analyses carried out in this paper are based on composite spectra, which should be highly insensitive to such a small change in sample size, we did not feel it necessary to re-perform these analyses and they are presented using the initially detected sample. This issue will not be present in the DESI DR2 Mg II absorber catalog when it is made publicly available.

In order to construct our composite spectrum, we must first select a suitable sample of absorbers from the full population of 545,905 absorbers initially detected in the DESI DR2 data. Firstly, we remove all associated absorption systems, that is absorbers with velocity offset values greater than 3500 km s^{-1} , as the restframe of these absorbers is similar to the restframe of their background QSOs, and the QSO emission lines present could influence the resulting composite spectrum.

Next, we make the choice to incorporate only QSO spectra in which a single Mg II absorber was detected. This ensures a smoother continuum in the resulting composite, as the effect of absorption lines from absorption systems at other redshifts, as well as the effect of the emission lines of each background QSO, should be minimized or mitigated entirely. Both of these features could

be amplified if we were to use QSO spectra in which multiple absorbers were detected, particularly at the edges of our redshift coverage where fewer spectra are available. These choices reduce our sample to 238,838 single intervening absorber QSO spectra.

Notably, we do not expect this latter choice, to use only QSO spectra in which a single Mg II absorber was detected, to affect the science results of this study, as the natures of all intervening absorption systems are similar, and the presence of multiple absorption systems in a single QSO spectrum is solely the result of the line of sight to the QSO. As such, this choice is made primarily to simplify the reduction of the composite spectrum, which we will detail in §2.3.

As the absorption systems present in these spectra have been identified using the Mg II absorption doublet at 2796Å 2803Å, and DESI spectra have an observed wavelength coverage of [3600Å, 9824Å], the range of possible absorption systems redshifts is $z_{\text{ABS}} \approx [0.3, 2.5]$. Figure 1 presents the redshift distribution for these absorbers. Fewer absorbers are detected at the low and high ends of this distribution due in large part to the underlying QSO redshift distribution in DESI, as well as increased noise at the edges of the DESI spectrum (e.g. Chaussidon et al. 2023). Additionally, there are slight dips in the distribution around $z \approx 1.1$ and $z \approx 1.8$, which we interpret to be due to the DESI spectrograph crossover regions (DESI Collaboration et al. 2016; Napolitano et al. 2023).

One relevant consideration in construction our sample is the distribution of Mg II rest-frame equivalent width values with respect to redshift. Generally, absorption line systems at low redshifts have smaller equivalent width values than those at higher redshifts (Lan & Fukugita 2017). As a result the absorbers that contribute to the reddest region of our composite will generally have lower equivalent width values than those that contribute to the bluest region. We choose not to make any selection on the rest-frame equivalent width in the interest of maximizing sample size.

Next, we construct a control sample of DESI QSOs without any detected Mg II absorbers. The total population of such objects in DESI DR2 is 2,061,617 spectra. From this sample we first remove the 25 percent of QSOs that have lowest g-band flux. This is done as the completeness of our Mg II detection approach is reduced for these fainter spectra (Napolitano et al. 2023), and as such we can be less confident that these spectra do not have undetected Mg II absorbers. Additionally, this cut results in the distributions of g-band flux values between QSO spectra with, and without, Mg II absorbers being in greater agreement as the population of spectra

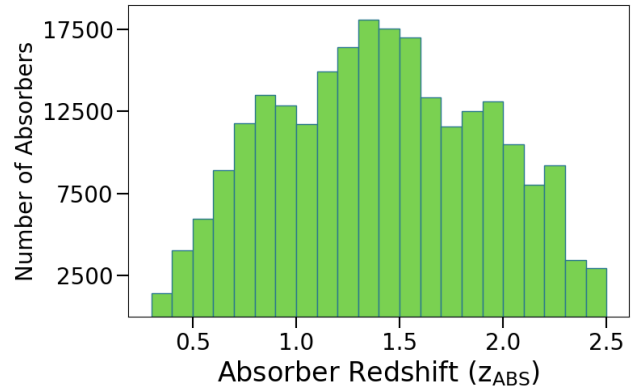


Figure 1. Histogram of absorber redshift values for the 238,838 absorption line systems in our sample. Bins are 0.1 wide in redshift space.

with detected absorbers tends to be brighter than that of spectra with no detected absorbers.

For each single-absorber QSO spectrum in our sample, we then select a matching control QSO spectrum. This selection is performed for each absorbed QSO spectrum by determining which DESI QSO with no detected Mg II absorbers minimizes the total difference in redshift and TSNR2_QSO value. TSNR2_QSO is a measurement of the signal-to-noise ratio of the spectrum, where certain regions are more heavily weighted according to the expected spectral characteristics of the target class (Guy et al. 2023b). Each control QSO spectrum is matched exclusively to a single-absorber QSO spectrum, i.e. each member of the control sample is unique. Comparison of this control sample will enable confirmation of the source of any features in the single-absorber composite spectrum, as well as aiding in the fitting of these features.

Figure 2 displays the distributions of multiple parameters of our absorber and control samples. Comparing them we can note that the absorber sample tends to have slightly higher values of QSO redshift and TSNR2_QSO . This is due to a bias in detecting Mg II absorbers, as QSOs above redshift $z = 2.1$ are targeted to receive additional observations in DESI (Myers et al. 2023). Multiple observations of the same object then increase signal-to-noise ratio, and make it easier to detect an absorption line system (Napolitano et al. 2023). Noting this, we consider our two samples to be in strong enough agreement to enable the analyses we perform in this paper.

2.2. Composite Construction

Having determined our sample of absorbed QSO spectra, as well as our control sample, we can now consider the methods by which we calculate the composite spectrum for each. As previously mentioned, the wavelength

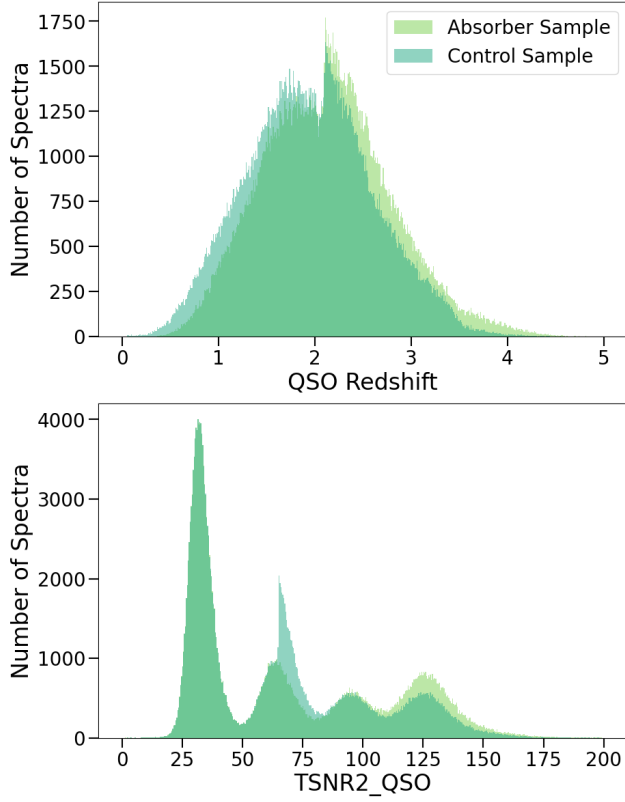


Figure 2. Histograms displaying the distributions of the redshift (top), TSNR2-QSO (middle) and W2 band flux values for both our absorber (light green) and control (blue) sample. Each histogram is drawn with 500 equally sized bins.

coverage of DESI spectra is $[3600\text{\AA}, 9824\text{\AA}]$ and the approximate redshift range of our absorption line systems is $z_{\text{ABS}} \approx [0.3, 2.5]$. As the rest-frame wavelength coverage of a $z_{\text{ABS}} = 0.3$ absorber is $\approx [2770, 7557]$, and that of a $z_{\text{ABS}} = 2.5$ absorber is $\approx [1028\text{\AA}, 2806\text{\AA}]$, this informs a natural wavelength range of $[1030\text{\AA}, 7500\text{\AA}]$ for our absorber restframe composite. Relatedly, we choose a pixel spacing of 0.4\AA , corresponding to the native DESI wavelength spacing of 0.8\AA , shifted into the rest-frame of a $z_{\text{ABS}} = 1.0$ absorption system, a value close to the center of our redshift distribution. Figure 3 shows the number of spectra that when shifted into the absorption restframe contribute to each pixel of the composite spectrum.

Next, we shift each spectrum in our sample into the restframe of its detected absorption system by dividing its wavelength coverage by $(1 + z_{\text{ABS}})$. We then resample the flux values of the spectrum onto the common rest-frame wavelength grid using the Python package `scipy.signal`, which utilizes FFT transformations to perform the resampling (Virtanen et al. 2020). In order to normalize our individual spectra, we divide by

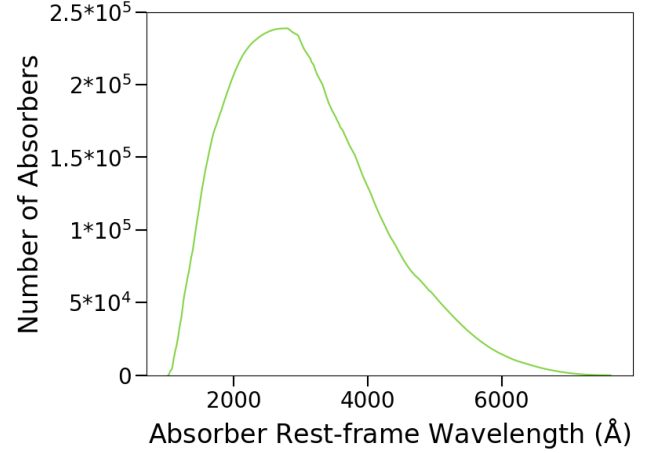


Figure 3. The number of spectra, that when resampled into the absorber restframe, cover each pixel of the composite’s wavelength grid. The distribution peaks in the range $[2795\text{\AA}, 2804\text{\AA}]$, which is the location of the Mg II doublet, and is available in the restframe of all 238,838 absorption systems.

the median flux in two regions immediately adjacent to the Mg II absorption doublet, $[2760\text{\AA}, 2780\text{\AA}]$ and $[2820\text{\AA}, 2840\text{\AA}]$. Both of these regions are available in the restframe for the majority of our sample, however at the edges of our redshift distribution only one may be present.

We perform this process of shifting into the restframe, resampling flux values, and normalizing via the regions adjacent to the Mg II absorption doublet for all 238,838 entries in our sample of QSO spectra that host one detected absorption line system. We then repeat this process for our control sample, using the absorption system redshift of the absorbed spectrum to which each control group member was matched. Finally, we calculate the median value in each pixel of our common rest-frame wavelength grid, producing our composite spectrum. We determine the error in our composite spectrum by taking the difference between the 16th and 84th percentile value in each pixel and dividing by the square root of the number of spectra which, when shifted into the restframe of the absorption system, cover that pixel, as shown in Figure 3.

In Figure 4, we present the results of this procedure for both our sample of spectra with a single detected absorption system, and our control sample. We can immediately note that the control sample composite is significantly brighter than the absorber sample composite at wavelengths less than 2000\AA , and slightly brighter at wavelengths greater than 5000\AA . A number of absorption lines are immediately evident in the absorber sample composite, including the Mg II doublet at $\sim 2800\text{\AA}$, C IV doublet at $\sim 1550\text{\AA}$ and a broad Lyman- α ab-

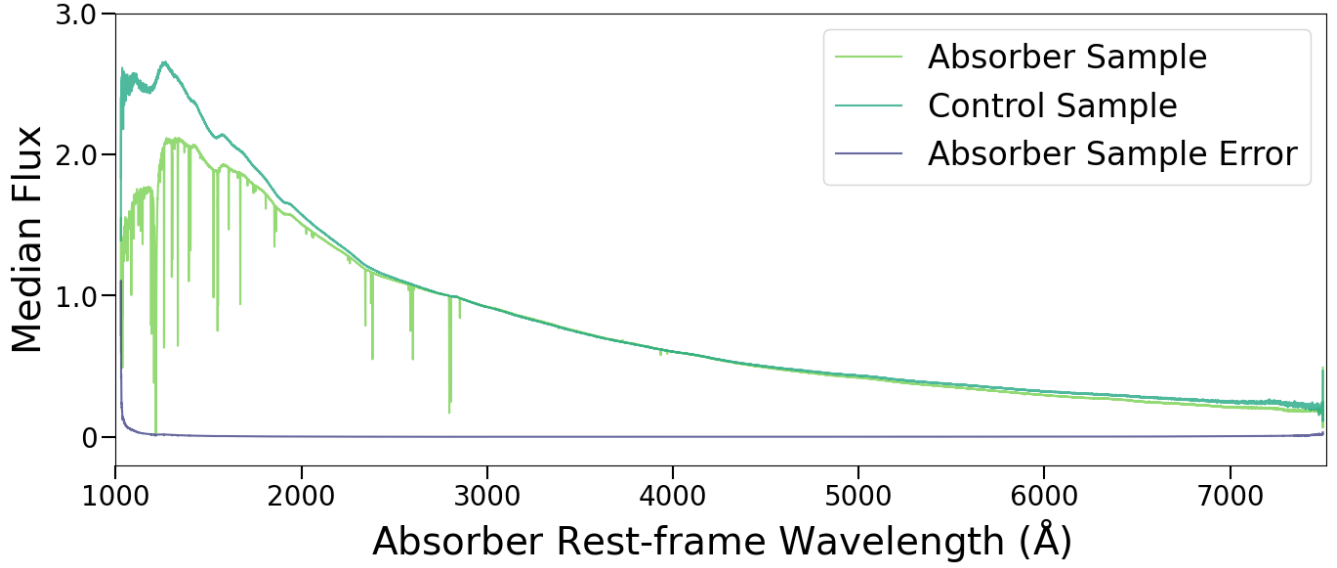


Figure 4. Median composite spectra calculated for both our sample of QSO spectra with a single detected Mg II absorber, and our matched control sample of QSO spectra with no detected absorbers. Also presented is the error spectrum associated with the absorber sample composite. Note that we do not show the error spectrum associated with the control sample, as the two error spectra would appear nearly identical.

sorption line at $\sim 1215\text{\AA}$. In the following subsection, we will detail the methods by which we identify and fit these lines, and the many additional lines that are present.

2.3. Composite Reduction & Line Fitting

Having calculated our composite spectrum, we can now consider the process of line identification. Rather than automating this step, we choose to perform a precise visual inspection, wherein the absorber sample composite was carefully scanned by eye in order to identify possible lines. Observed lines were then identified, and confirmed, using resources such as atomic spectra atlases, like those provided by Morton (1991, 2003) and Kramida et al. (2024), as well as lists of absorption lines from similar projects and references therein (e.g. Lu & Savage 1993; Vanden Berk et al. 2001; Pieri et al. 2010). Note that hereafter we will refer to Morton (2003) as M03 and Kramida et al. (2024) simply as NIST.

In total we observe 72 unique absorption lines, arising from 26 unique absorption species. Additionally, we observe 7 *emission* lines corresponding to the transitions: [O II], H γ , H β , [O III] and H α .

In order to cleanly fit these atomic lines, we will need to normalize our composite spectrum, for which we can utilize the control sample composite detailed in §2.2. As previously noted, the overall shape, ignoring absorption species, of the control and “absorber” composite spectra are quite similar, however the control sample composite is significantly brighter at wavelengths less than 2000\AA . **This difference in brightness is due to reddening**

from the dust associated with the absorbing gas, details regarding the magnitude of this absorption can be found in Napolitano et al. (2025).

To better fit the control sample composite to the absorber composite, we first divide the absorber sample composite by the control sample composite, resulting in the spectrum seen in the top panel of Figure 5. We then mask all pixels within 10\AA of all detected emission and absorption lines, increasing this to 40\AA for the broader Lyman- α line.

Next, we fit a cubic B-spline, as implemented in the Python package SciPy, to the masked composite spectrum. The resulting fit can be seen in the middle panel of Figure 5 (Virtanen et al. 2020). In order to avoid overfitting or underfitting the masked composite, we must carefully choose a smoothness value for our spline. We do so by testing a range of possible values, and calculating the sum of squared differences from a $y = 1$ line in the previously masked regions around our detected emission and absorption lines. We find that this quantity steadily decreases with increased smoothing, up to a value of 1.1, at which point further smoothing has little effect in the line regions, and instead begins to underfit the broad features of the composite continuum. For this reason, we select a smoothing value for our spline of $s = 1.1$.

By then dividing the absorber sample composite by the product of our spline fit and the control sample composite, we successfully reduce our absorber sample composite, such that it is suitable for line fitting. This

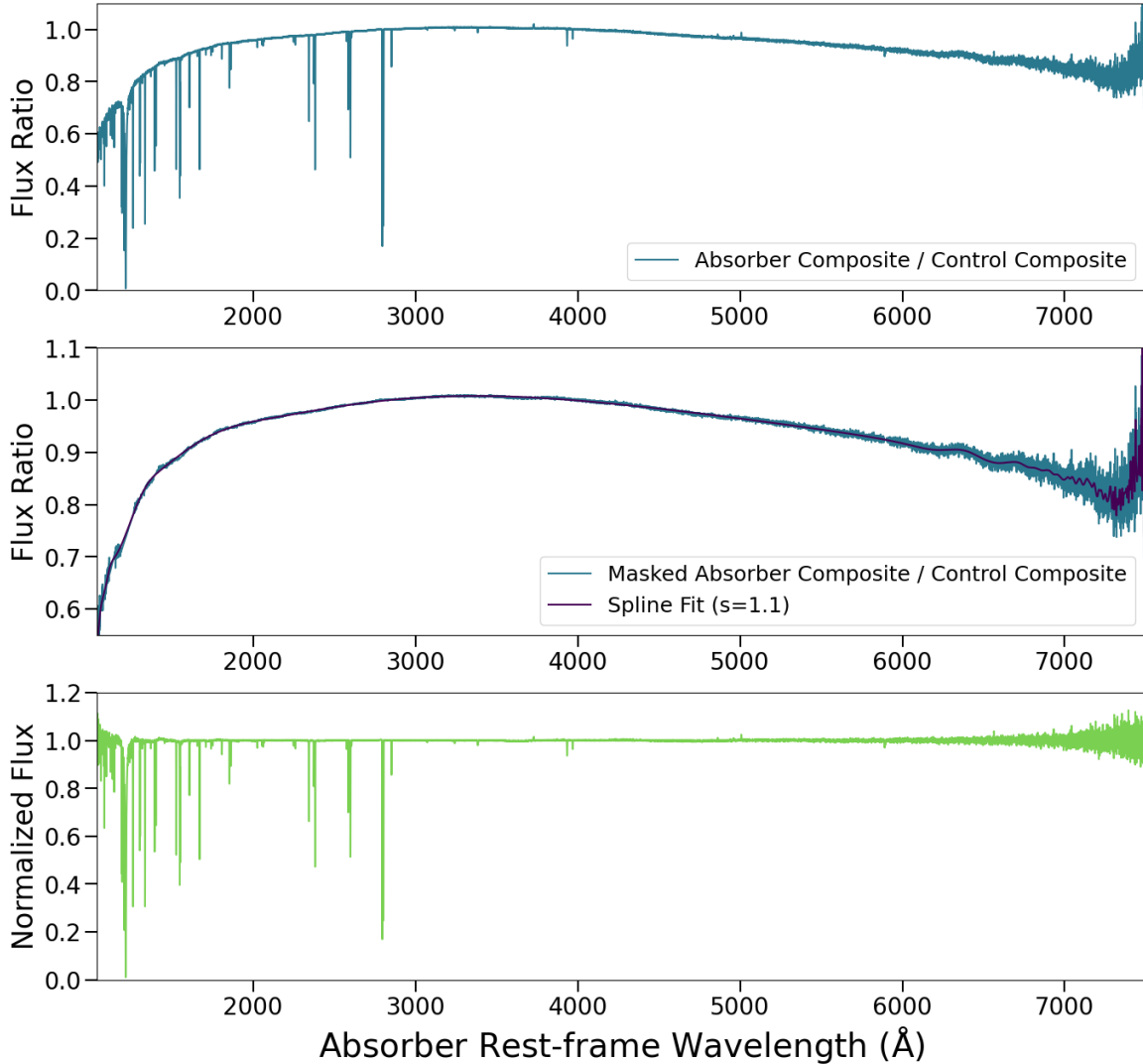


Figure 5. Visualization of the absorber sample continuum reduction method. *Top:* The result of dividing the absorber sample composite by the control sample composite, as seen in Figure 4. *Middle:* The result of masking the regions around the detected absorption and emission lines as described in the text. The purple line then shows the result of fitting a cubic B-spline with smoothness = 1.1 to the masked data. *Bottom:* The continuum-reduced absorber composite, calculated by dividing the product of the spline fit from the middle panel and the initial control sample composite.

reduced composite spectrum can be seen in the bottom panel of Figure 5 and a zoomed in and labeled version of this spectrum is shown in Figure 6.

Having now reduced our absorber composite spectrum, we can consider the matter of line fitting. We have designed our own line-fitting procedure, in which the majority of lines are fit using a single `Gaussian1D` model, as implemented in `Astropy`, which is initialized at the catalog wavelength of the atomic line (Astropy Collaboration et al. 2022). For lines whose catalog wavelength values are within 4.0\AA of a second line, such as the C IV and [O II] doublets, or O I 1302\AA and Si II 1304\AA , we instead use a compound model composed of two `Gaussian1D` models. The lines in the region around

Lyman- α require a special case solution: first, due to its width, we fit the Lyman- α line itself using a `Voigt1D` profile, and then form a compound model that includes all other lines in the region from 1200 to 1255\AA . A visualization of the output of our line fit procedure for all detected lines is shown in Figure 7.

After fitting each line, we record the parameters of the fit, as well as calculating the equivalent width of the line. In order to determine the uncertainties in these values, we draw 10,000 resampled composite spectra according to the error spectrum associated with our reduced absorber composite and perform our fit procedure, again recording the line parameters and equivalent width. In the next section we will detail the results of this process

and discuss our full atlas of observed absorption and emission lines.

3. RESULTS AND DISCUSSION

3.1. Line Fitting Results

The fit line centroid values and W_0 values for all fit line species are shown alongside their catalog vacuum wavelength and oscillator strength values in Tables 1 and 2. All vacuum wavelengths and oscillator strength values are sourced from NIST when available. Section §3.2 details which lines are instead sourced from M03 due to data availability. We can immediately note that the uncertainties in W_0 are highest at the edges of the wavelength coverage of the composite, and steadily decrease approaching the Mg II lines, which have extremely precise measurements. Examining the W_0 values, we note that the Lyman- α line is by far the strongest, and other strong lines include the Mg II doublet (2796Å, 2803Å), Si III 1206Å, the C IV doublet (1548Å, 1550Å), and O VI 1032Å, although this line has large uncertainties. The centroids of all fit lines are within 1Å of the reference value, and many are within 0.1Å or less, suggesting that our fits are reliable and species identifications accurate.

We note that our list contains a number of blended line systems, these include both multiplet blends such as N I 1134Å, N I 1200Å and Ti II 1910Å as well as inter-species blends such as lines we observe at 2026Å and 2062Å, which are composed of Zn II, Cr II, Mg I and Cr II and Zn II respectively. For each of these blends, the table wavelength we provide is an un-weighted average of the components. However we do provide the oscillator strength values for each component line as well as the individual vacuum wavelength values in a table footnote.

Examining the complete list of fit lines, we can observe that all detected absorption species are transitions from the ground state, suggesting that there is not a significant ionizing radiation background present in the absorbing gas. At least, there is not one capable of producing excited states that would result in additional absorption lines visible in the optical. Previous studies have detected O VIII and Ne IX absorption in CGM-like gas [Nicastrro et al. \(e.g. 2002, 2005\)](#). It is worth considering then, that the gas that produces the absorption lines we observe may not be co-spatial with the absorbing gas. Certainly they are at similar redshifts, and are likely to be associated with the same galactic environment, but the regions in which they arise are likely to be distinct.

3.2. Challenging Line Identifications

While examining our full sample of absorption lines, we encountered a number of challenges in identification.

Here we will document the natures of these challenges, as well as explain our reasoning for assigning a given identification.

Firstly, we considered two possible identifications from G03 for the line we observe at 1039Å, either O I 1039.2304Å or Fe II 1039.3128Å. Both are transitions from the ground state, however the Fe II line does not appear on NIST. Additionally, the centroid of our Gaussian line fit is 1039.208Å, which is in better agreement with the O I line; for these reasons we adopt this identification.

Concerning the line we observe at 1122Å, we considered three possible identifications from G03, C I 1122.2597Å, C I 1122.437Å and Fe III 1122.5183Å. Of these, the latter two are transitions from the ground state, however the excited state line C I 1122.2597Å is in best agreement with our fit centroid value. Finding it very unlikely that this line could result from an excited state, since as previously noted all other detected lines are associated with transitions from the ground state, we have decided on an identification of C I 1122.437Å, as it is in closer agreement with the fit line centroid compared to Fe III 1122.5183Å.

Finally, we can consider the lines we detect at 1454Å and 1709Å. In both cases we considered two possible identifications, a Ni II line listed in G03, but not found on NIST (1454.842Å and 1709.6042Å respectively), and an Fe II line (1454.838Å and 1709.5543Å respectively). Despite reservations due to the inability to find the Ni II lines on NIST, we ultimately choose to adopt these identifications, as both Fe II lines are transitions from an excited state, and therefore we find them very unlikely. Notably the Ni II 1454Å line is not present in the finding list for interstellar lines in QSO spectra from [York et al. \(2006, their Table A2\)](#), however the Ni II 1709Å line is present.

3.3. Examining Emission Line Detection

As the emission features we detect in our composite have not been observed to the same signal-to-noise ratio in previously constructed composite spectra, we consider their observation worthy of additional investigation. Firstly, to demonstrate definitively that these emission lines are a feature of the intervening absorption systems, we will analyze composites constructed using only high v_{off} systems. Then we will consider how the detectability of these emission features scales with the number of Mg II absorbers used in the construction of the composite.

When selecting our sample, we choose to use any absorber with $v_{\text{off}} > 3,500 \text{ km s}^{-1}$, a fairly canonical value for the separation of intervening and associated absorp-

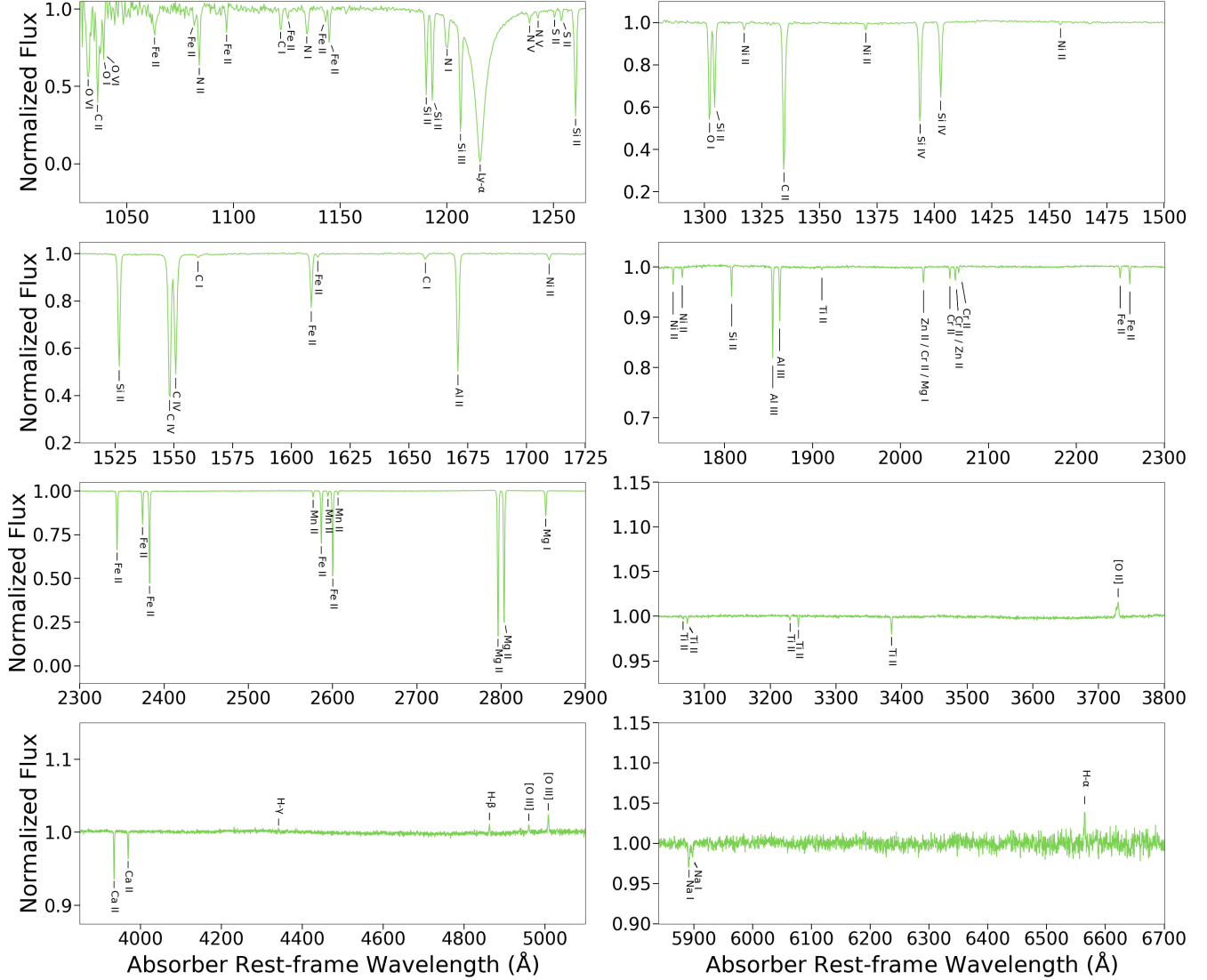


Figure 6. Labeled and horizontally stretched version of the reduced absorber sample median composite spectrum, as plotted in Figure 5. Detected absorption and emission lines are labeled, and lines that are blends of multiple species have each species listed. Note that the scale on both axes varies.

tion systems (e.g. York et al. 2006; Zhu & Ménard 2013; Khare et al. 2014; Chen et al. 2020; Anand et al. 2021). However, this value was commonly thought to be larger in past studies (see discussion in Shen & Ménard 2012), and even considering the present value there are environments, such as large galaxy groups, in which emission not arising from the absorbing gas could be co-spatial with it.

To verify that the emission lines we detect are truly associated with the absorption line systems, and not the QSO host galaxy, or any nearby group member, we construct two sub-samples, one composed of systems with $v_{\text{off}} > 50,000 \text{ km s}^{-1}$, and a second composed of systems with $v_{\text{off}} > 100,000 \text{ km s}^{-1}$.

These specific thresholds are chosen arbitrarily, and the resulting sub-samples contain 56.4% ($N = 134,610$) and 22.2% ($N = 53,060$) of the full sample respectively. Considering the $v_{\text{off}} > 50,000 \text{ km s}^{-1}$ sub-sample, we can note that the median background QSO redshift in this sample is $z_{\text{QSO}} = 2.324$, and the median absorption system redshift is $z_{\text{ABS}} = 1.244$. In a Λ CDM cosmology with $H_0 = 69.6 \text{ km s}^{-1} \text{ Mpc}^{-1}$, $\Omega_M = 0.286$ and $\Omega_\Lambda = 0.714$, these redshift values correspond to a difference in comoving radial distance of $\sim 1800 \text{ Mpc}$, a distance far too great for any causal effect between the background QSO and foreground absorber (Wright 2006; Bennett et al. 2014). This difference in comoving radial distance determined by the median QSO and absorber system

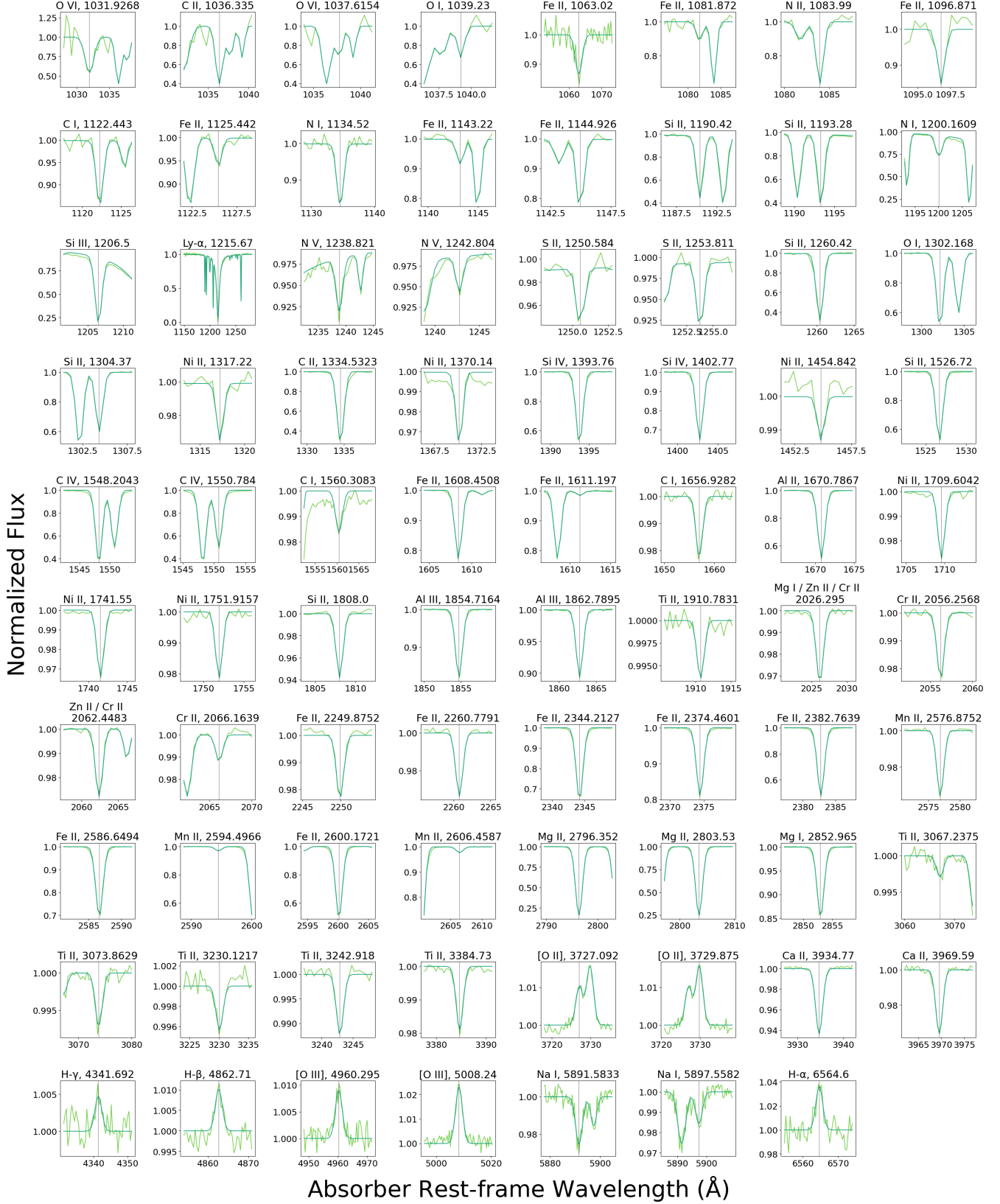


Figure 7. Grid view of the output of our line fitting procedure. A subplot is drawn for each noted absorption or emission line. The absorber composite is shown in light green, and the model fit shown in blue. Each line is plotted in a 10σ range around its centroid value. Subplots are titled by the line's vacuum wavelength, as given in Tables 1 & 2.

redshift values increases to ~ 2666 Mpc for the $v_{\text{off}} > 100,000$ km s $^{-1}$ sub-sample.

Using these sub-samples we then construct composite spectra and plot the emission line regions in Figure 8. We can immediately note that the emission features are nearly identical in all three composites, clearly confirming that these features are indeed associated with the absorption systems.

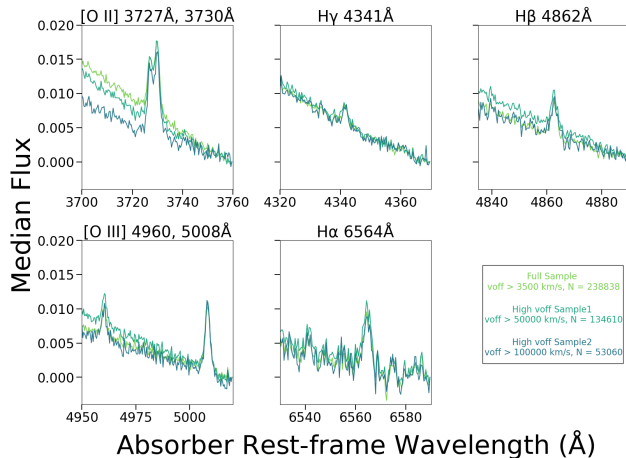


Figure 8. The regions of the composite spectrum featuring emission features. Composites are plotted for the full sample as well as two high v_{off} sub-samples as indicated in the legend in the bottom right. Note that the y-axis has been arbitrarily rescaled so as to enable comparison between the different composites.

Next, we consider the detectability of these emission features. Specifically we will consider the [O II] doublet at 3727Å, 3730Å, as it is both the strongest emission feature by equivalent width in the reduced composite, and it is covered by the largest fraction of the sample, as can be seen in Figure 3. All absorbers at redshifts $0.3 < z_{\text{ABS}} < 1.6$ when shifted into their restframe will cover the [O II] doublet; the total number of such systems is 154,138, $\sim 64.5\%$ of our total sample. From this we draw random samples of smaller numbers of absorption systems and compute composite spectra. These composites are collectively shown in Figure 9. We observe that the [O II] emission doublet is indistinguishable from the noise in composites having less than $N = 5,000$ spectra, and that the doublet only begins to be well-resolved with $N \sim 10,000$ spectra. Here we can clearly see the increase in signal-to-noise ratio gained by constructing an absorber composite spectrum with such a large sample.

Having demonstrated both that the emission features we detect are related to the absorption systems, and that their extremely low signal likely made them unde-

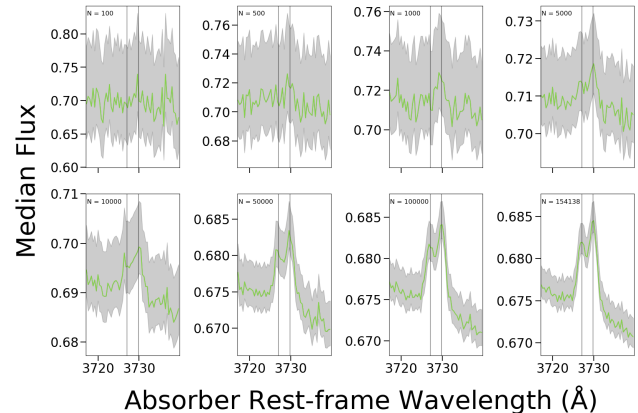


Figure 9. The [O II] doublet, 3727Å, 3729Å], as resolved in composite spectra constructed with a varying number of absorption systems. The number of systems contributing to each composite is shown in the upper left hand of each sub-plot. The central green line is the median composite spectrum, and the gray bands show the error in the composite measurement. Note that the y-scale changes significantly between panels.

tectable in many previously constructed composites, we consider our detection to be extremely robust.

4. CONCLUSION

In this paper we have described the construction and analysis of a composite spectrum of QSO absorption line systems using a catalog of Mg II absorbers identified in spectra from the second data release (DR2) of DESI. We have outlined the methods by which we constructed our sample of 238,838 absorbers, considering only those QSO spectra with a single identified Mg II absorber at $v_{\text{off}} > 3,500$ km s $^{-1}$. We further construct a control sample of QSO spectra with no detected Mg II absorbers, by matching to our absorbed sample on the basis of QSO redshift and signal-to-noise ratio.

For both our absorbed QSO and control QSO sample, we have calculated median spectra in the restframe of the detected absorption systems. We have outlined the necessary procedures including the resampling of flux values on a common wavelength grid from [1030Å, 7500Å] with a 0.4Å spacing and the normalization of individual spectra using the average flux in regions adjacent to the Mg II absorption doublet. The resulting composite spectra are presented in Figure 4.

We have then detailed the methods by which we searched for absorption features in the absorber sample composite spectrum, finding a total of 72 absorption lines from 26 atomic species. We also identify 7 emission lines, associated with the [O II], Hγ, Hβ, [O III] and Hα transitions. Some of these features, particularly [O II], have been observed and utilized in previous stud-

ies of absorber composite spectra (e.g. Wild et al. 2007; Ménard et al. 2011; Zhu & Ménard 2013; Khare et al. 2014; Joshi et al. 2018), whereas others ($H\beta$, $H\gamma$) have only been previously observed in QSO-galaxy pairs (e.g. York et al. 2012; Straka et al. 2013, 2015). Here we produce the highest signal-to-noise ratio measurement of these lines in an absorber composite spectrum presently available. In order to fit the lines we observe, we first estimate a continuum for our absorbed sample composite spectrum using the control sample composite spectrum and a cubic b-spline fit.

We have detailed the methods by which we fit the resulting reduced absorber composite, and the results of this line-fitting procedure are presented in our full line atlas (Tables 1 and 2). We further describe the process by which we derive line identifications, relying primarily on Morton (2003) and Kramida et al. (2024). We have noted how we made identifications for some challenging lines. Finally, we carefully verified that the emission lines we observed in our absorber composite are genuinely at the same redshift as the gas associated with the absorbers, by constructing composites only at very high v_{off} . We then also examined the increase in signal-to-noise of the [O II] doublet with increasing sample size, demonstrating that the emission features present in this composite would not have been readily detectable in many previous absorber composite studies. The details presented in the paper provide the most complete study of the composite spectrum of QSO absorption line systems in the wavelength range [1030 Å, 7500 Å] to date, and should aid in further studies of the physical natures of these absorbers. Furthermore, our analysis here provides an opportunity to better model absorption line systems, and understand their impact on studies of the Lyman- α forest, and other studies of the spectra of QSOs. In future work we intend to examine the composites formed when binning absorbers based on their W_0 values, and to construct similar composites for the DESI DR3 sample, when made available.

ACKNOWLEDGMENTS

LN and ADM were supported by the U.S. Department of Energy, Office of Science, Office of High Energy Physics, under Award Number DE-SC0019022.

This material is based upon work supported by the U.S. Department of Energy (DOE), Office of Science, Office of High-Energy Physics, under Contract No. DE-AC02-05CH11231, and by the National Energy Research Scientific Computing Center, a DOE Office of Science User Facility under the same contract. Additional support for DESI was provided by the U.S. National Science Foundation (NSF), Division of Astronomical Sciences under Contract No. AST-0950945 to the NSF’s National Optical-Infrared Astronomy Research Laboratory; the Science and Technology Facilities Council of the United Kingdom; the Gordon and Betty Moore Foundation; the Heising-Simons Foundation; the French Alternative Energies and Atomic Energy Commission (CEA); the National Council of Humanities, Science and Technology of Mexico (CONAH-CYT); the Ministry of Science, Innovation and Universities of Spain (MICIU/AEI/10.13039/501100011033), and by the DESI Member Institutions: <https://www.desi.lbl.gov/collaborating-institutions>. Any opinions, findings, and conclusions or recommendations expressed in this material are those of the author(s) and do not necessarily reflect the views of the U. S. National Science Foundation, the U. S. Department of Energy, or any of the listed funding agencies.

The authors are honored to be permitted to conduct scientific research on I’oligam Du’ag (Kitt Peak), a mountain with particular significance to the Tohono O’odham Nation.

The data used to construct the Figures in this paper are available on Zenodo at DOI: [10.5281/zenodo.XXXXXX](https://doi.org/10.5281/zenodo.XXXXXX)

REFERENCES

- Alam, S., Aubert, M., Avila, S., et al. 2021, *PhRvD*, **103**, 083533
- Alexander, D. M., Davis, T. M., Chaussidon, E., et al. 2023, *AJ*, **165**, 124
- Anand, A., Nelson, D., & Kauffmann, G. 2021, *MNRAS*, **504**, 65
- Astropy Collaboration, Price-Whelan, A. M., Lim, P. L., et al. 2022, *ApJ*, **935**, 167
- Bahcall, J. N., & Spitzer, Lyman, J. 1969, *ApJL*, **156**, L63
- Bennett, C. L., Larson, D., Weiland, J. L., & Hinshaw, G. 2014, *ApJ*, **794**, 135
- Brotherton, M. S., Tran, H. D., Becker, R. H., et al. 2001, *ApJ*, **546**, 775
- Chaussidon, E., Yèche, C., Palanque-Delabrouille, N., et al. 2023, *ApJ*, **944**, 107
- Chen, Z.-F., Qin, H.-C., Chen, Z.-G., et al. 2020, *ApJ*, **893**, 25
- Corlies, L., Peeples, M. S., Tumlinson, J., et al. 2020, *ApJ*, **896**, 125

- Corlies, L., & Schiminovich, D. 2016, *ApJ*, **827**, 148
- DESI Collaboration, Aghamousa, A., Aguilar, J., et al. 2016, arXiv e-prints, arXiv:1611.00037
- DESI Collaboration, Abareshi, B., Aguilar, J., et al. 2022, *AJ*, **164**, 207
- DESI Collaboration, Adame, A. G., Aguilar, J., et al. 2025a, in preparation
- DESI Collaboration, Abdul-Karim, M., Aguilar, J., et al. 2025b, arXiv e-prints, arXiv:2503.14738
- Fawcett, V. A., Alexander, D. M., Brodzeller, A., et al. 2023, *MNRAS*, **525**, 5575
- Francis, P. J., Hewett, P. C., Foltz, C. B., et al. 1991, *ApJ*, **373**, 465
- Frank, S., Rasera, Y., Vibert, D., et al. 2012, *MNRAS*, **420**, 1731
- Gallagher, S. C., Hines, D. C., Blaylock, M., et al. 2007, *ApJ*, **665**, 157
- Guy, J., Bailey, S., Kremin, A., et al. 2023a, *AJ*, **165**, 144
- . 2023b, *AJ*, **165**, 144
- Joshi, R., Srianand, R., Petitjean, P., & Noterdaeme, P. 2018, *MNRAS*, **476**, 210
- Khare, P., Berk Daniel, V., Rahmani, H., & York, D. G. 2014, *ApJ*, **794**, 66
- Kramida, A., Yu. Ralchenko, Reader, J., & and NIST ASD Team. 2024, NIST Atomic Spectra Database (ver. 5.12), [Online]. Available: <https://physics.nist.gov/asd> [2025, June 28]. National Institute of Standards and Technology, Gaithersburg, MD.
- Lan, T.-W. 2020, *ApJ*, **897**, 97
- Lan, T.-W., & Fukugita, M. 2017, *ApJ*, **850**, 156
- López, G., & Chen, H.-W. 2012, *MNRAS*, **419**, 3553
- Lu, L., & Savage, B. D. 1993, *ApJ*, **403**, 127
- Matthews, T. A., & Sandage, A. R. 1963, *ApJ*, **138**, 30
- Ménard, B., Wild, V., Nestor, D., et al. 2011, *MNRAS*, **417**, 801
- Miller, T. N., Doel, P., Gutierrez, G., et al. 2024, *AJ*, **168**, 95
- Morton, D. C. 1991, *ApJS*, **77**, 119
- . 2003, *ApJS*, **149**, 205
- Mullaney, J. R., Alexander, D. M., Goulding, A. D., & Hickox, R. C. 2011, *MNRAS*, **414**, 1082
- Myers, A. D., Moustakas, J., Bailey, S., et al. 2023, *AJ*, **165**, 50
- Napolitano, L., Pandey, A., Myers, A. D., et al. 2023, *AJ*, **166**, 99
- Napolitano, L., Myers, A. D., Fawcett, V. A., et al. 2025, *AJ*, **170**, 16
- Nicastro, F., Zezas, A., Drake, J., et al. 2002, *ApJ*, **573**, 157
- Nicastro, F., Mathur, S., Elvis, M., et al. 2005, *Nature*, **433**, 495
- Pieri, M. M., Frank, S., Weinberg, D. H., Mathur, S., & York, D. G. 2010, *ApJL*, **724**, L69
- Poppett, C., Tyas, L., Aguilar, J., et al. 2024, *AJ*, **168**, 245
- Richards, G. T., Lacy, M., Storrie-Lombardi, L. J., et al. 2006, *ApJS*, **166**, 470
- Sambruna, R. M., Maraschi, L., & Urry, C. M. 1996, *ApJ*, **463**, 444
- Schlafly, E. F., Kirkby, D., Schlegel, D. J., et al. 2023, *AJ*, **166**, 259
- Schmidt, M. 1963, *Nature*, **197**, 1040
- Selsing, J., Fynbo, J. P. U., Christensen, L., & Krogager, J. K. 2016, *A&A*, **585**, A87
- Shen, Y., & Ménard, B. 2012, *ApJ*, **748**, 131
- Sprayberry, D., & Foltz, C. B. 1992, *ApJ*, **390**, 39
- Straka, L. A., Whichard, Z. L., Kulkarni, V. P., et al. 2013, *MNRAS*, **436**, 3200
- Straka, L. A., Noterdaeme, P., Srianand, R., et al. 2015, *MNRAS*, **447**, 3856
- Tumlinson, J., Peebles, M. S., & Werk, J. K. 2017, *ARA&A*, **55**, 389
- Vanden Berk, D., Khare, P., York, D. G., et al. 2008, *ApJ*, **679**, 239
- Vanden Berk, D. E., Richards, G. T., Bauer, A., et al. 2001, *AJ*, **122**, 549
- Virtanen, P., Gommers, R., Oliphant, T. E., et al. 2020, *Nature Methods*, **17**, 261
- Wagoner, R. V., Fowler, W. A., & Hoyle, F. 1967, *ApJ*, **148**, 3
- Wijers, N. A., & Schaye, J. 2022, *MNRAS*, **514**, 5214
- Wild, V., Hewett, P. C., & Pettini, M. 2007, *MNRAS*, **374**, 292
- Wright, E. L. 2006, *PASP*, **118**, 1711
- Wu, X., Cai, Z., Lan, T. W., et al. 2025, *ApJ*, **983**, 186
- York, D. G., Khare, P., Vanden Berk, D., et al. 2006, *MNRAS*, **367**, 945
- York, D. G., Straka, L. A., Bishof, M., et al. 2012, *MNRAS*, **423**, 3692
- Zheng, W., Kriss, G. A., Telfer, R. C., Grimes, J. P., & Davidsen, A. F. 1997, *ApJ*, **475**, 469
- Zhu, G., & Ménard, B. 2013, *ApJ*, **770**, 130

Table 1. Absorption Lines Observed in Absorber Composite

Vacuum		Oscillator	Observed	
Wavelength (Å)	Species	Strength (f_{ik})	Wavelength (Å)	W_0 (Å)
1031.9268	O VI	1.33E-1	1031.950	$1.413^{+0.416}_{-0.212}$
1036.335	C II	1.19E-1	1036.384	$1.310^{+0.154}_{-0.294}$
1037.6154	O VI	6.60E-2	1037.754	$0.858^{+0.534}_{-0.181}$
1039.230	O I	9.16E-3	1039.208	$0.756^{+0.144}_{-0.256}$
1063.020	Fe II	1.4E-2	1062.980	$0.807^{+0.111}_{-0.138}$
1081.872	Fe II	1.3E-2	1081.805	$0.543^{+0.108}_{-0.088}$
1083.990	N II	1.11E-1	1083.962	$0.951^{+0.038}_{-0.054}$
1096.871	Fe II	3.3E-2	1096.796	$0.541^{+0.052}_{-0.043}$
1122.443	C I	1.27E-3	1122.264	$0.699^{+0.039}_{-0.038}$
1125.442	Fe II	1.6E-2	1125.694	$0.603^{+0.103}_{-0.150}$
1134.520	N I ^a	1.46E-2/2.87E-2/4.16E-2	1134.553	$0.838^{+0.032}_{-0.029}$
1143.220	Fe II	1.9E-2	1143.203	$0.495^{+0.044}_{-0.038}$
1144.926	Fe II	8.3E-2	1144.962	$0.704^{+0.021}_{-0.024}$
1190.42	Si II	2.77E-1	1190.400	$1.208^{+0.010}_{-0.010}$
1193.28	Si II	5.75E-1	1193.294	$1.281^{+0.009}_{-0.009}$
1200.161	N I ^b	1.32E-1/8.69E-2/4.32E-2	1200.089	$1.021^{+0.015}_{-0.014}$
1206.51	Si III	1.67E0	1206.510	$1.463^{+0.008}_{-0.007}$
1215.673	Ly α	4.164E-1	1215.659	$9.416^{+0.033}_{-0.034}$
1238.804	N V	1.56E-1	1238.864	$0.502^{+0.031}_{-0.034}$
1242.795	N V	7.80E-2	1242.755	$0.336^{+0.035}_{-0.030}$
1250.5834	S II	6.02E-3	1250.553	$0.301^{+0.035}_{-0.024}$
1253.813	S II	1.21E-2	1253.764	$0.418^{+0.021}_{-0.020}$
1260.42	Si II	1.22E0	1260.397	$1.430^{+0.007}_{-0.007}$
1302.168	O I	5.20E-2	1302.171	$1.127^{+0.007}_{-0.006}$
1304.37	Si II	9.28E-2	1304.366	$0.999^{+0.008}_{-0.007}$
1317.22	Ni II ^c	-	1317.255	$0.290^{+0.028}_{-0.023}$
1334.5323	C II	1.29E-1	1334.546	$1.469^{+0.005}_{-0.005}$
1370.14	Ni II	-	1370.124	$0.289^{+0.026}_{-0.019}$
1393.76	Si IV	5.13E-1	1393.763	$1.176^{+0.005}_{-0.004}$
1402.77	Si IV	2.55E-1	1402.770	$0.970^{+0.005}_{-0.005}$
1454.842	Ni II	1.9E-3	1454.829	$0.160^{+0.021}_{-0.020}$
1526.72	Si II	1.33E-1	1526.707	$1.149^{+0.003}_{-0.003}$
1548.2043	C IV	1.90E-1	1548.210	$1.500^{+0.003}_{-0.003}$
1550.784	C IV	9.52E-2	1550.770	$1.311^{+0.003}_{-0.003}$
1560.3083	C I	7.16E-2	1560.227	$0.365^{+0.012}_{-0.057}$
1608.4508	Fe II	5.91E-2	1608.452	$0.772^{+0.004}_{-0.005}$
1611.197	Fe II	1.4E-3	1611.223	$0.202^{+0.025}_{-0.021}$
1656.9282	C I	1.43E-1	1656.997	$0.306^{+0.014}_{-0.013}$
1670.7867	Al II	1.77E0	1670.788	$1.189^{+0.003}_{-0.003}$
1709.6042	Ni II	2.6E-3	1709.569	$0.278^{+0.011}_{-0.011}$
1741.55	Ni II	-	1741.561	$0.239^{+0.011}_{-0.011}$
1751.9157	Ni II	-	1751.955	$0.239^{+0.011}_{-0.011}$

Table 1 *continued*

Table 1 (*continued*)

Vacuum		Oscillator	Observed	
Wavelength (Å)	Species	Strength (f_{ik})	Wavelength (Å)	W_0 (Å)
1808.00	Si II	2.49E-3	1808.003	$0.393^{+0.006}_{-0.006}$
1854.7164	Al III	5.61E-1	1854.719	$0.732^{+0.003}_{-0.003}$
1862.7895	Al III	2.79E-1	1862.799	$0.558^{+0.004}_{-0.004}$
1910.7831	Ti II ^d	1.04E-1	1910.719	$0.143^{+0.015}_{-0.017}$
2026.295	Zn II/Cr II/Mg I ^e	5.01E-1/1.30E-3/1.13E-1	2026.202	$0.328^{+0.006}_{-0.006}$
2056.2568	Cr II	1.03E-1	2056.244	$0.253^{+0.007}_{-0.007}$
2062.4483	Cr II/Zn II ^f	7.59E-2/2.46E-1	2062.383	$0.294^{+0.007}_{-0.006}$
2066.1639	Cr II	5.12E-2	2066.155	$0.179^{+0.009}_{-0.010}$
2249.8752	Fe II	1.82E-3	2249.877	$0.263^{+0.006}_{-0.006}$
2260.7791	Fe II	2.44E-3	2260.771	$0.318^{+0.005}_{-0.005}$
2344.2127	Fe II	1.14E-1	2344.213	$1.083^{+0.002}_{-0.002}$
2374.4601	Fe II	3.59E-2	2374.463	$0.793^{+0.002}_{-0.002}$
2382.7639	Fe II	3.20E-1	2382.766	$1.324^{+0.002}_{-0.002}$
2576.8752	Mn II	3.58E-1	2576.880	$0.351^{+0.004}_{-0.004}$
2586.6494	Fe II	7.17E-2	2586.649	$1.028^{+0.002}_{-0.002}$
2594.4966	Mn II	2.79E-1	2594.499	$0.326^{+0.004}_{-0.004}$
2600.1721	Fe II	2.39E-1	2600.174	$1.334^{+0.001}_{-0.002}$
2606.4587	Mn II	1.96E-1	2606.462	$0.280^{+0.005}_{-0.005}$
2796.352	Mg II	6.08E-1	2796.354	$1.875^{+0.001}_{-0.001}$
2803.530	Mg II	3.03E-1	2803.533	$1.726^{+0.001}_{-0.001}$
2852.965	Mg I	1.80E0	2852.962	$0.745^{+0.002}_{-0.002}$
3067.2375	Ti II	4.89E-2	3067.066	$0.122^{+0.015}_{-0.018}$
3073.8629	Ti II	1.21E-1	3073.807	$0.180^{+0.009}_{-0.009}$
3230.1217	Ti II	6.87E-2	3230.106	$0.120^{+0.013}_{-0.015}$
3242.9180	Ti II	2.32E-1	3242.921	$0.204^{+0.007}_{-0.007}$
3384.7300	Ti II	3.58E-1	3384.722	$0.279^{+0.006}_{-0.007}$
3934.77	Ca II	6.82E-1	3934.760	$0.559^{+0.005}_{-0.005}$
3969.59	Ca II	3.3E-1	3969.551	$0.427^{+0.006}_{-0.006}$
5891.5853	Na I	6.41E-1	5891.529	$0.466^{+0.029}_{-0.112}$
5897.5582	Na I	3.20E-1	5897.410	$0.338^{+0.039}_{-0.086}$

^a Blend of N I lines: 1134.165 Å, 1134.415 Å, 1134.980 Å.^b Blend of N I lines: 1199.550 Å, 1200.223 Å, 1200.710 Å.^c Note that oscillator strength values are not available on NIST for many of the Ni II lines we observe.^d Blend of Ti II lines: 1910.6123 Å, 1910.9538 Å.^e Blend of Zn II 2026.1371 Å, Cr II 2026.271 Å, Mg I 2026.477 Å.^f Blend of Cr II 2062.2360 Å, Zn II 2062.6604 Å.

Table 2. Emission Lines Observed in Absorber Composite

Vacuum		Oscillator	Observed	
Wavelength (Å)	Species	Strength (f_{ik})	Wavelength (Å)	W_0 (Å)
3727.092	[O II]	3.31E-13	3727.091	$0.250^{+0.021}_{-0.018}$
3729.875	[O II]	8.95E-14	3729.886	$0.304^{+0.014}_{-0.016}$
4341.692	H γ	4.469E-2	4341.403	$0.147^{+0.023}_{-0.031}$
4862.71	H β	1.194E-1	4862.638	$0.265^{+0.018}_{-0.019}$
4960.295	[O III]	2.81E-14	4960.277	$0.270^{+0.026}_{-0.025}$
5008.240	[O III]	1.32E-13	5008.346	$0.422^{+0.015}_{-0.015}$
6564.60	H α	6.411E-1	6564.633	$0.479^{+0.043}_{-0.046}$